SNR and Dose Considerations for ^{129}Xe Magnetic Resonance Spectroscopy

by

Haoran Dai

Graduate Program in Medical Physics
Duke University

Date: _____

Approved:

_____
Bastiaan Driehuys, Supervisor

_____
David Mummy

_____
Scott Robertson

_____
Timothy Turkington

Thesis submitted in partial fulfillment of
the requirements for the degree of Master of Science in the
Graduate Program in Medical Physics
in the Graduate School
of Duke University

2023

ABSTRACT

SNR and Dose Considerations for ^{129}Xe Magnetic Resonance Spectroscopy

by

Haoran Dai

Graduate Program in Medical Physics
Duke University

Date: _____

Approved:

_____
Bastiaan Driehuys, Supervisor

_____
David Mummy

_____
Scott Robertson

_____
Timothy Turkington

An abstract of a thesis submitted in partial fulfillment of
the requirements for the degree of Master of Science in the
Graduate Program in Medical Physics
in the Graduate School
of Duke University

2023

Abstract

Hyperpolarized (HP) ^{129}Xe Magnetic Resonance Imaging (MRI) is a promising approach for the non-invasive diagnosis of pulmonary pathophysiology and has recently received FDA approval. This technique has emerged as a valuable tool that holds significant potential for non-invasive investigation of various lung disorders. HP ^{129}Xe MRI is typically utilized to evaluate regional pulmonary ventilation and gas exchange functions.

Hyperpolarized (HP) ^{129}Xe MR spectroscopy has emerged as an equally valuable addition to the repertoire of imaging diagnostic tools available. The application of HP ^{129}Xe MR spectroscopy enables us to investigate blood oxygenation levels, as evidenced through ^{129}Xe red blood cell (RBCs) shifts. It also provides an insight into hemodynamics through cardiogenic oscillations of ^{129}Xe-RBC signal amplitudes.

Despite its potential clinical utility, the use of HP ^{129}Xe MR spectroscopy has been limited by the lack of established standards for measuring and interpreting its signal quality. In particular, there is currently no consensus on how to calculate the signal-to-noise ratio (SNR) of HP ^{129}Xe spectroscopic data or how to determine the appropriate dose of HP ^{129}Xe necessary to achieve high-quality NMR signals suitable for clinical analysis.

To address these issues, this study developed a reliable approach in calculating the ^{129}Xe MR spectroscopic SNR from clinical data using recommended acquisition protocols. We focused on developing a method for estimating the SNR that takes into account the inherent variability of HP ^{129}Xe signals and the effects of noise and artifacts, such as those arising from cardiogenic signal oscillations, in the acquired data. Our method involves acquiring multiple repetitions of the HP ^{129}Xe signal and using a combination of statistical techniques and signal processing algorithms to estimate the SNR from the resulting time series data.

In addition to developing a method for calculating the HP ^{129}Xe SNR, we also investigated the relationship between the administered dose equivalent of the HP ^{129}Xe and the resulting SNR. By acquiring NMR signals over a range of doses, we were able to establish a quantitative relationship between dose and SNR that can be used to guide the selection of an appropriate HP ^{129}Xe dose for a given clinical application. Moreover, our investigation identified definitive thresholds for the requisite SNR and dosage required to obtain high-quality static measurements of RBC/Membrane ratio, RBC chemical shifts, and dynamic measurements of RBC amplitude oscillations through HP ^{129}Xe MRS. In conjunction with a recent evaluation that assessed scan quality in our laboratory using a 5-point Likert scale, our study provides significant empirical data for guiding clinical practice.

Overall, our approach represents an important step towards standardizing the use of HP ^{129}Xe MR spectroscopy in clinical practice. Through the provision of a trustworthy and quantitative measurement of SNR, as well as the establishment of a clear correlation between dosage and SNR, our study ensures that the acquisition and analysis of HP ^{129}Xe MRS scan is executed in a consistent and reproducible manner across different institutions and studies.

Besides its potential impact on clinical practice across different sites, this study also has implications for ongoing research efforts. By providing a more robust method for measuring signal quality, this study will be helpful to facilitate future studies aimed at advancing our understanding of the underlying physiology of pulmonary disease and evaluating the efficacy of new treatments.

Contents

List of Figures

Acknowledgements

I would like to express my gratitude to Bastiaan Driehuys, my advisor, for his invaluable mentorship, guidance, and support. His extensive expertise, profound knowledge, insightful feedback, and wise counsel have been a constant source of inspiration to me throughout my academical and professional journey. I would also like to thank David Mummy for his guidance and for organizing the thought-provoking weekly lab discussions on image analysis that have enriched my research experience. I wish to extend my appreciation to our team for providing me a great learning experience and expanding my research perspectives. Finally, I would like to thank Scott Robertson and Timothy Turkington for serving on my thesis committee.

1. Introduction

The recent approval of Xenoview by the Food and Drug Administration (FDA) marks a significant milestone in the development of drug and device combinations that utilize hyperpolarized (HP) ^{129}Xe Magnetic Resonance Imaging (MRI). This innovative technology offers radiologists a new option for assessing lung ventilation in patients 12 years and older, both in the adult and pediatric population. Hyperpolarized (HP) ^{129}Xe MR imaging is a valid modality that allows for noninvasive measurement of pulmonary physiology. The predominant approach to hyperpolarized-gas MRI of the lung is through ventilation imaging, which entails the capture of a series of two-dimensional images, or a three-dimensional image set following inhalation of the gas, during a breath-hold interval. In normally functioning areas of the lung, ventilation images display amplified signal levels; however, ventilation defects, which are characterized by the absence or reduced signal levels, are evident in areas where airflow is partially or completely obstructed. The technique has shown significant potential for the diagnosis and monitoring of a variety of pulmonary diseases, such as chronic obstructive pulmonary disease (COPD) and asthma, as illustrated in the accompanying Figure 1.

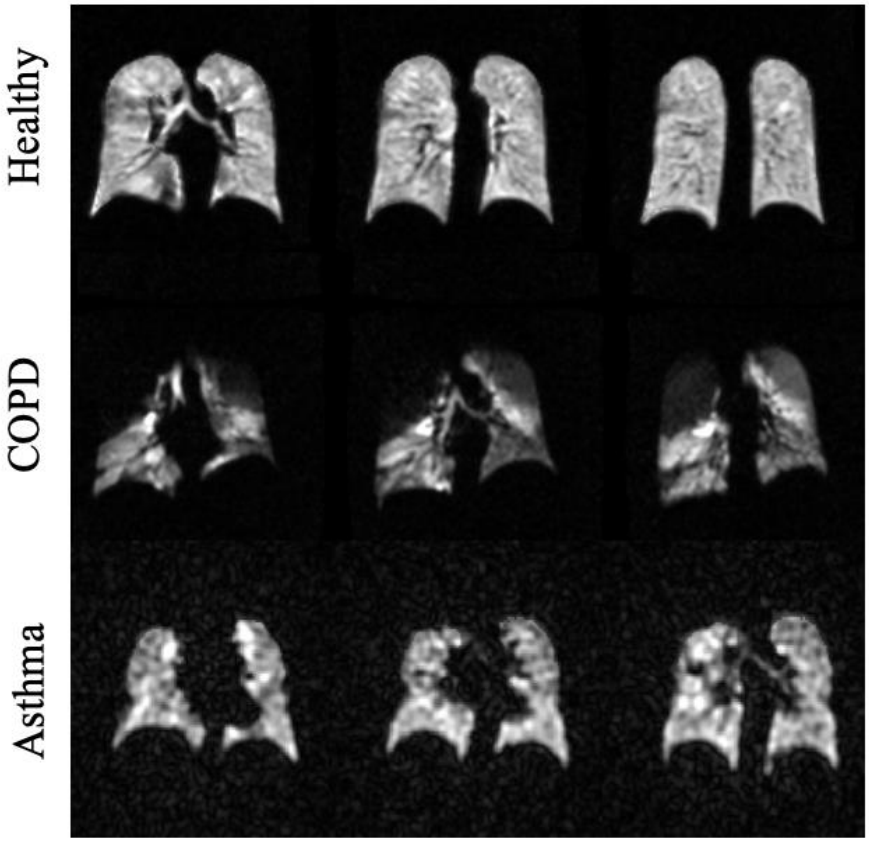

Figure 1: Gradient echo ventilation imaging of diseased human lung acquired using hyperpolarized ^{129}Xe. Ventilation images acquired in healthy subject (first row), and COPD subject (second row).

Upon administration of the HP ^{129}Xe atoms into the respiratory system, they move through the bronchial airway tree into the alveoli and air spaces inside the alveolar ducts, where it freely diffuses across the membrane and into the RBCs, as shown in Figure 2. These inherent characteristics of ^{129}Xe gas, in conjunction with its chemical shifts, make it uniquely suited for assessing pulmonary gas exchange.

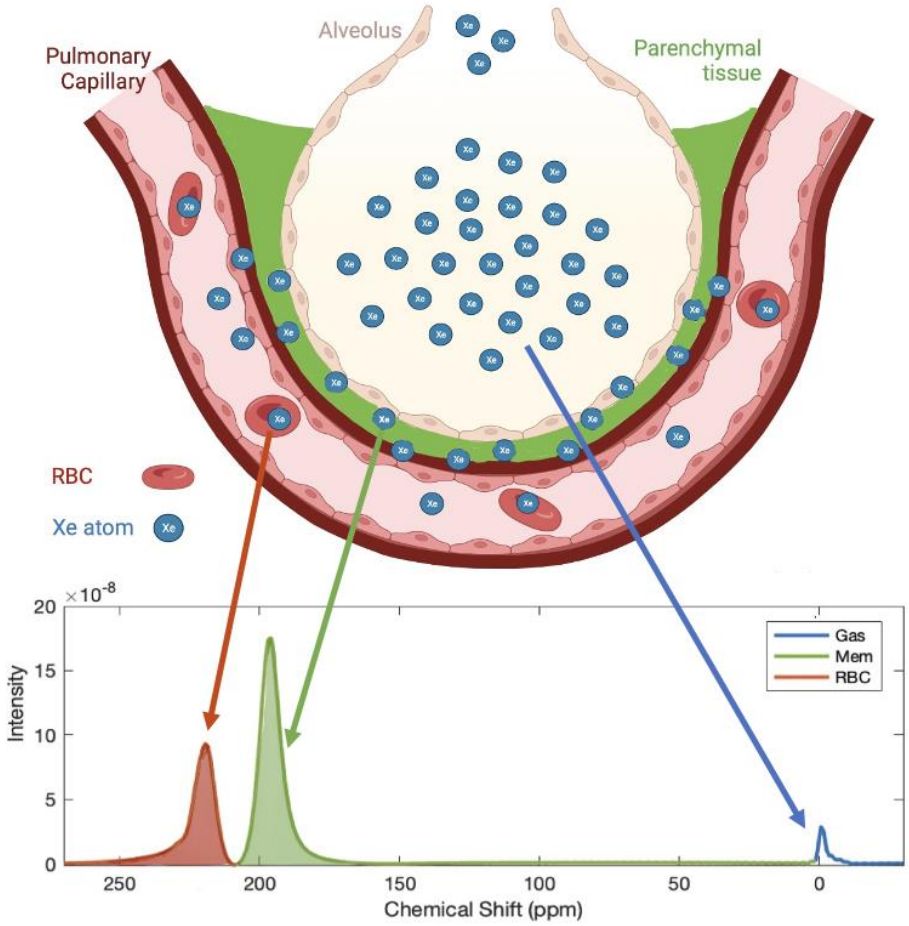

Figure 2: Gas Exchange Mechanism: ^{129}Xe diffusion follows a similar pathway to that of oxygen and has chemical shifts that enable it to be distinguished in each compartment.

The regional pulmonary gas exchange function is evaluated based on its nuclear magnetic resonance (NMR) signal composition, including the gaseous phase signal within the alveolar ducts and the dissolved phase signals in lung parenchymal tissues, blood plasma, and red blood cells. The employment of regional dissolved phase imaging has revealed discernible discrepancies in diverse disease, age, and gender groups. The latest investigations on this biomarker have illustrated distinctions in obstructive and restrictive

pulmonary ailments, such as, chronic obstructive pulmonary disease (COPD), idiopathic fibrosis (IPF), pulmonary artery hypertension (PAH), as visually represented in the corresponding Figure 3. The utilization of this dissolved phase imaging leverages these characteristics to facilitate the 3D visualization of ^{129}Xe distribution in airspace (ventilation), membrane uptake, and RBC transfer. These maps are color-coded to distinguish between various signal intensity levels. Specifically, defects are designated with the color red, low intensity regions with orange, two bins adjacent to the mean of the reference population with green, and higher intensity areas with blue. As the membrane maps, the first four color coincided with those of the ventilation and RBC maps. However, in order to visually distinguish the elevated membrane signal typically found in individuals with idiopathic pulmonary fibrosis (IPF), the highest bins were allocated the colors pink and purple.

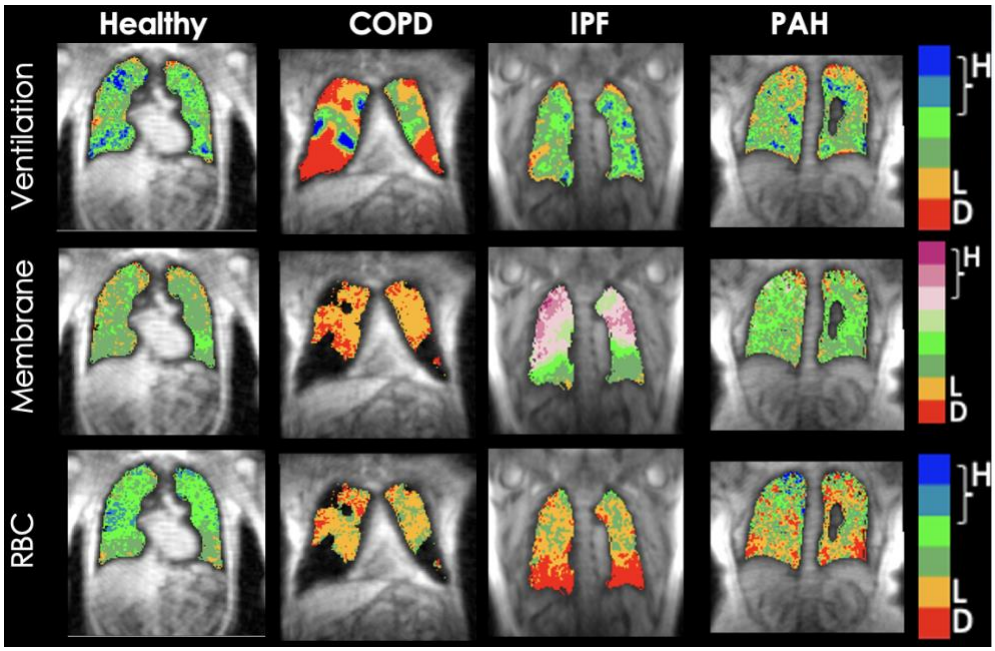

Figure 3: Dixon gas- and dissolved phase imaging of human lungs acquired using hyperpolarized ^{129}Xe. Gas exchange imaging acquired in healthy subject, chronic obstructive pulmonary disease (COPD) patient, idiopathic pulmonary fibrosis (IPF) patient, and pulmonary artery hypertension (PAH) patient [1].

In addition to HP ^{129}Xe imaging, HP ^{129}Xe Magnetic Resonance Spectroscopy has been recognized as a valuable modality that has the ability to quantitatively measure gas exchange function. HP ^{129}Xe MR spectroscopy, as shown in Figure 4, allows for investigation of blood oxygenation levels as indicated through ^{129}Xe red blood cell shifts, as well as provides an insight into hemodynamics. The capacity of HP ^{129}Xe MRS to quantify these biometrics facilitates the detection of pulmonary abnormalities and enables the diagnosis of various respiratory disorders. The ratio of ^{129}Xe-RBC to ^{129}Xe-membrane, which includes parenchyma tissues and blood plasma, has been identified as a highly reliable metric for ^{129}Xe gas exchange, and it shows promising potential as a

sensitive indicator of gas exchange dysfunction in patients with idiopathic pulmonary fibrosis (IPF) [2,3]. With further investigations conducted in our laboratory, researchers are enhancing their understanding of the association of this biometric with hemoglobin levels.

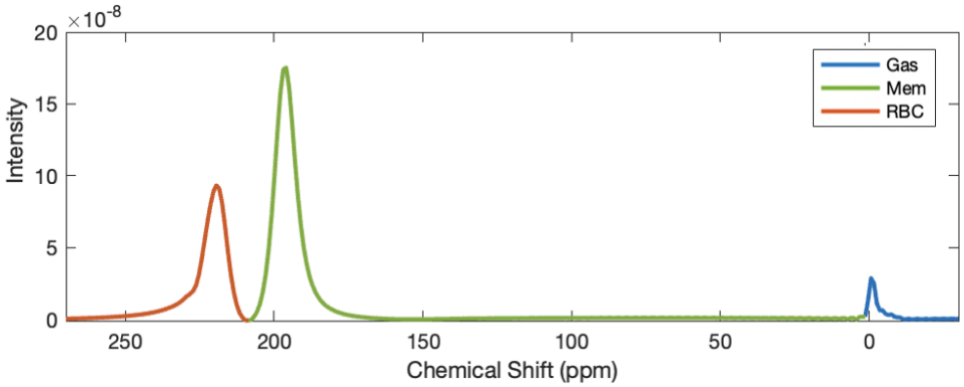

Figure 4: Static Magnetic Resonance Spectroscopy of gas- and dissolved phase hyperpolarized ^{129}Xe.

The dissolved phase HP ^{129}Xe NMR signals exhibit unique resonance frequency shifts, also known as chemical shifts, which arise from the diamagnetic susceptibility effects at the atomic level caused by large, loosely bound electron clouds of Xenon atoms. In a healthy individual HP ^{129}Xe chemical shifts typically amount to 0 ppm in the gas component, approximately 218 ppm in the RBC component and 198 ppm in the membrane component. Studies have revealed that HP ^{129}Xe chemical shifts in RBCs exhibit a nonlinear variation with blood oxygenation levels [4], as shown in Figure 5. This characteristic makes HP ^{129}Xe MRS a promising noninvasive tool for evaluating oxygenation concentration in pulmonary blood. Determination of the tissue and blood

oxygenation concentration provides critical insights into various pulmonary pathologies. Hypoxia can impact the functionality and the lifespan of neutrophils that contribute to lung inflammation [5], in the cases of asthma and chronic obstructive pulmonary disease (COPD).

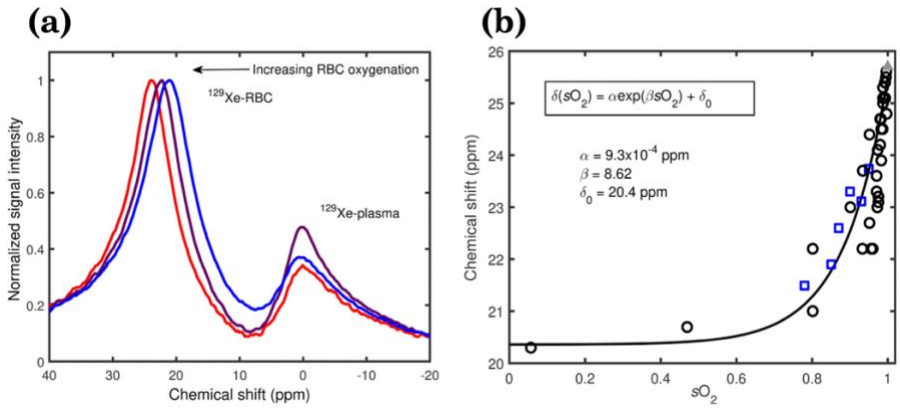

Figure 5: Pulmonary capillary blood oxygenation characterized by ^{129}Xe-RBC chemical shifts. (a) ^{129}Xe-blood spectra acquires at 3T. With increasing oxygenation, the peak associated with ^{129}Xe-RBC resonance shifts towards a higher frequency. (b) An exponential relationship between oxygenation saturation and ^{129}Xe-RBC chemical shift. G. Leung, N.J. Stewart et al., Magnetic Resonance in Medicine, 2017 [4].

Furthermore, the temporal pattern of the oscillations of ^{129}Xe-RBC and ^{129}Xe-Membrane signals have been observed to closely approximate the frequency of cardiac pulsation. In our laboratory, investigation into the interaction between ^{129}Xe and RBC provides a unique avenue for identifying diverse cardiopulmonary disorders [6], as shown in Figure 6. Specifically, the resulting signal demonstrates cardiac oscillations that enable differentiation between pre- and post- capillary pulmonary hypertension (PH). PH results from tiny pulmonary arteries and arterioles contracting, remodeling, and thrombosing [7]. PH is frequently misidentified as other heart and lung ailments,

owing to its non-specific symptoms, which can result in delayed diagnosis [8]. The complex pathophysiology underlying PH makes it difficult to diagnose and monitor, as there are no definite biometrics available [9]. This noninvasive HP ^{129}Xe MRS approach to PH detection holds particular importance given the invasive nature of the conventional heart catheterization (RHC) procedure, which has been associated with adverse health effects [10].

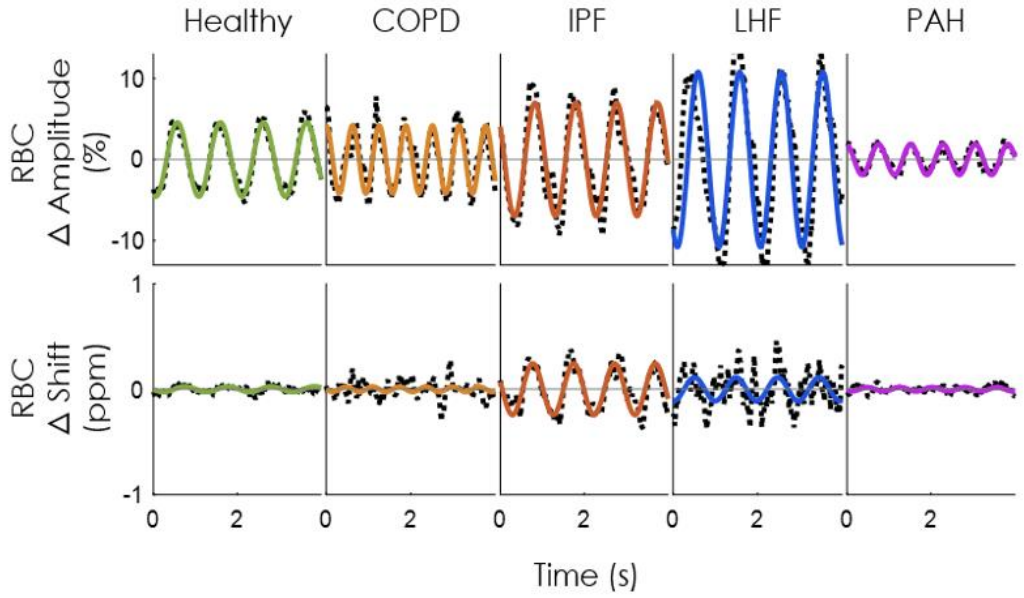

Figure 6: Cardiogenic oscillations of healthy subjects and patients across disease groups. Elevated RBC amplitude oscillations in left heart failure (LHF), whereas those in pulmonary artery hypertension (PAH) display a decline. Wang, Bier et al., Eur Resp J. 2018 [1].

Despite the promise of HP ^{129}Xe MRS probing biomarkers associated with lung pathological functions, it has been hindered by a lack of standardization in signal measurement and interpretation. Without established protocols for assessing signal quality, it is difficult to compare results across studies or between institutions.

Additionally, the optimal dose of HP ^{129}Xe MRS scans for generating high quality spectra remains uncertain, potentially limiting the widespread use of this technique. Addressing these limitations will be crucial to realizing the full potential of HP ^{129}Xe MRS as a non-ionizing diagnostic modality for pulmonary diseases. In this study, our efforts focus on standardizing protocols for signal interpretation and determining the minimum effective dose of HP ^{129}Xe for generating high-quality spectra. By establishing these standards, researchers and clinicians can more effectively utilize this promising technique in pulmonary diseases diagnosis and management.

2. Background

2.1 Nuclear Magnetic Resonance Physics

In magnetic resonance imaging and spectroscopy, the nuclei (HP ^{129}Xe) exhibit nuclear magnetic resonance (NMR) activity. This requirement is contingent upon the presence of a non-zero spin in the nuclei, which indicates an odd number of neutrons and/or an odd number of protons. The symmetrization postulate provides support for this condition. Following the symmetrization postulate, a system of identical particles is required to have a quantum state vector that is either symmetric or antisymmetric with respect to exchange of any pair of particles. Proved by relativistic quantum mechanics, the symmetrization postulate indicates that fermions are supposed to have antisymmetric states while bosons are supposed to have symmetric states [11]. The symmetrization postulate is more commonly known as Pauli exclusion principle, stating that no two identical fermions can occupy the same quantum state (spin state) at the same time. Thus, in an atom, pairs of nucleons' spins tend to align in opposite directions such that their magnetic moments cancel. When an atom consists of an even number of protons and an even number of neutrons, the aggregate spin of the atom is completely canceled, resulting in a total spin of zero. Conversely, atoms that contain an odd number of protons and/or neutrons have a non-zero spin, as complete cancellation of the spin cannot be achieved.

Nuclei that exhibit NMR activity, including but not limited to ^{1}H, ^{13}C, ^{31}P, and ^{19}F, possess spin 1/2, rendering them particularly advantageous over other levels of spin, such as 1 and 3/2, which are associated with shorter T2 relaxation times. In clinical MRI, ^{1}H is the most prevalent nucleus utilized, as it is abundantly present in human tissue. However, proton MRI/MRS scans of the lungs are challenging due to the limited proton density in pulmonary region, leading to a reduction in signal intensity. Conventional proton scans only provide anatomical information and not pulmonary functions. An optimal choice for monitoring pulmonary functions is the gaseous form of HP ^{129}Xe, which possesses a spin of ½, high solubility in pulmonary tissues, blood, and its distinctive chemical shifts. Despite its low density and resulting difficulty in detection, 129Xe gas remains a desirable signal agent. This is due to the hyperpolarization technique outlined in section 2.2, which can effectively increase the polarization levels of the gas and mitigate effects of its low density, thereby enhancing the resulting signal. This explains why HP ^{129}Xe gas with spin ½ is the preferred signal agent in pulmonary MRI/MRS.

The microscopic magnetic moment μ that an NMR active nucleus possesses is given by:

$$\mu = \gamma J, \qquad (2.1)$$

where J stands for the angular momentum of this nucleus and γ stands for the gyromagnetic ratio. For ^{1}H, $\frac{\gamma}{2\pi} = 42.58\ MHz/T$. For ^{129}Xe, $\frac{\gamma}{2\pi} = -11.78\ MHz/T$.

In the presence of an external magnetic field applied by the MR scanner, the nuclear spin of an NMR active atom associated with angular momentum of its nucleons couples to the applied field and energy levels of the atom further divide into Zeeman level structure. This is known as the Zeeman effect. The potential energy of a magnetic moment vector μ in an external field vector B with magnitude B0 is given by:

$$E = -\gamma B = m_s \hbar B_0 \quad , \qquad (2.2)$$

where m_s stands for spin magnetic quantum number, and Plank's constant $\hbar$ is $1.05457 \times 10^{-34} J/Hz$.

For an atom, m_s can be $\pm 1/2$. This indicates that the Zeeman effect splits one signal spin state into two Zeeman levels with the higher energy level of spin (spin-down state) antiparallel to the external field and the lower energy of spin (spin-up state) parallel to the external field. In theory, the spin-up state with lower energy is energetically preferable. Yet not all atoms can attain this favorable state owing to the considerable thermal jostling energy ($k_B T$) that surpasses the Zeeman energy, thereby leading to a competition between the two. Due to the random thermal energy which attempts to distribute nuclei evenly between the two Zeeman levels, the ratio between numbers of nuclei spin-up (N_{up}) and the number of nuclei spin-down (N_{down}) is derived with Boltzmann statistics and given by:

$$\frac{N_{up}}{N_{down}} = e^{-\frac{\gamma \hbar B_0}{k_B T}}, \qquad (2.3)$$

where k_B is the Boltzmann constant, T is the temperature, and γ is the gyromagnetic ratio, a constant intrinsic to each different nucleus.

The nuclear magnetic resonance (NMR) signal is directly proportional to the disparity in the quantities of spin-up and spin-down. This disparity is well described by the concept of polarization (P), given by:

$$P = \frac{N_{up} - N_{down}}{N_{up} + N_{down}}, \qquad (2.4)$$

Polarization (P) refers to the proportion of nuclei that are available for magnetic resonance. In other words, the percentage of the excess spin-ups that are not canceled out in a collection.

For thermal equilibrium, the polarization is given by:

$$P = \frac{N_{up} - N_{down}}{N_{up} + N_{down}} \approx \frac{\gamma \hbar B_0}{2 k_B T}, \qquad (2.5)$$

In this context, it is possible to approximate the thermal polarization of ^{129}Xe nuclei that occurs during the respiratory process of patients within a 3T scanner to be approximately 2.8×10^{-6}.

We can then express the bulk magnetization in terms of polarization level:

$$M_0 = \frac{N_s \gamma \hbar}{2} P, \qquad (2.6)$$

where Ns is the number of net spin density.

As shown in equation (2.5), it is apparent that the magnitude of the bulk magnetization detected in MRI/S is directly proportional to the level of polarization exhibited by ^{129}Xe nuclei. Through the implementation of the hyperpolarization

technique, which is detailed in section 2.2, we are able to achieve polarization levels on order of 10^{-1} for ^{129}Xe nuclei produced within our laboratory. This translates to a substantial enhancement factor of five orders of magnitude, or 100,000 times higher, when compared to the polarization levels attainable through thermal equilibrium. Such high polarization overcomes the low density of the gas relative to tissues and provides sufficient signal for rapid high-resolution imaging.

2.2 Highly Polarized ^{129}Xe Production Technique

Hyperpolarized (HP) ^{129}Xe of spin ½ is produced through a process called spin exchange optical pumping (SEOP) with alkali metal vapor (rubidium vapor). The high-volume production method was developed by Driehuys et al. (1996) [12]: A mixture of high-pressure Xe, He, and N_2 gas flows into the polarizer, going through rubidium (Rb) vapors, into the optical pumping chamber. This is where SEOP happens.

Figure 7: The Polarizer used in our laboratory.

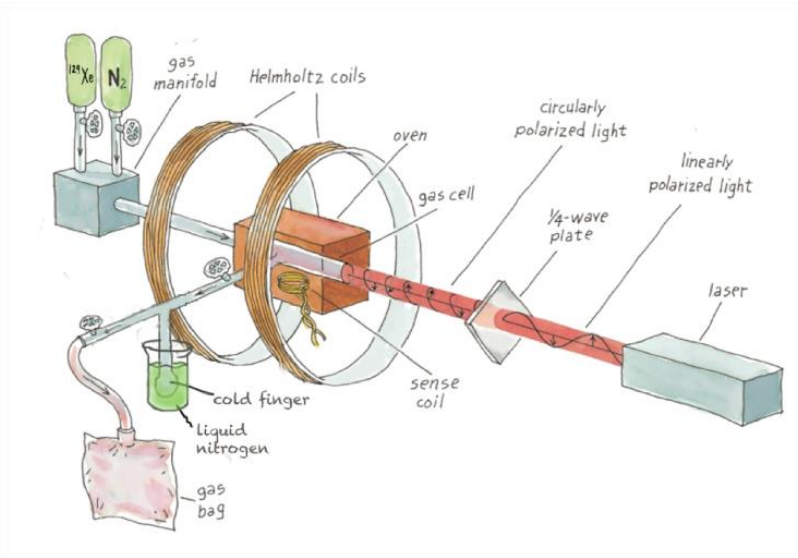

Figure 8: A simplified schematic sketch of ^{129}Xe polarizer [13].

The initial SEOP process involves the preparation of optically pumped Rb vapor. This process utilizes circularly polarized laser light to induce changes in the population distribution of atoms. Specifically, optical pumping is a technique for modifying the relative populations of Zeeman and hyperfine levels for ground-state atoms [14]. In our highly polarized ^{129}Xe production, collisional pressure broadening results in the complete elimination of the hyperfine structure, leaving only the simple spin of the atom – a $5^2S_{1/2}$ ground state with two spin sub levels and a $5^2P_{1/2}$ excited state with two sub-levels. Through optical pumping, the angular momentum of the circular polarized light is transferred to the electron spin of alkali metal Rb vapors. In our laboratory, this is achieved by tuning a laser of a wavelength of 795 nm from an AlGaAs laser diode in resonance with D1 transition [12]. The high-power laser diode is the primary factor in facilitating the polarization of significant amounts of Rb, thus leading to an increase in the throughput.

The valence electrons of Rb will be pumped from the $5^2S_{1/2}$ to $5^2P_{1/2}$ energy level, as indicated in Figure 9, which shows an external magnetic field splitting the $5^2S_{1/2}$ and $5^2P_{1/2}$ energy levels into two sub-Zeeman levels respectively. Figure 9 shows the optical pumping with left circularly polarized light with angular momentum of ħ typically. The two ground sub levels have the same energy as one another and the two excited state ones have the same as one another. This transition shown conserves both energy and angular momentum and that's why it doesn't get depleted. This is called "depletion

optical pumping". Thus, we have a steady-state Rb electron spin polarization on m_j = -1/2 level with continuous optical pumping. Note that we could also do the same with right circularly polarized light and thereby populate the +1/2 state instead.

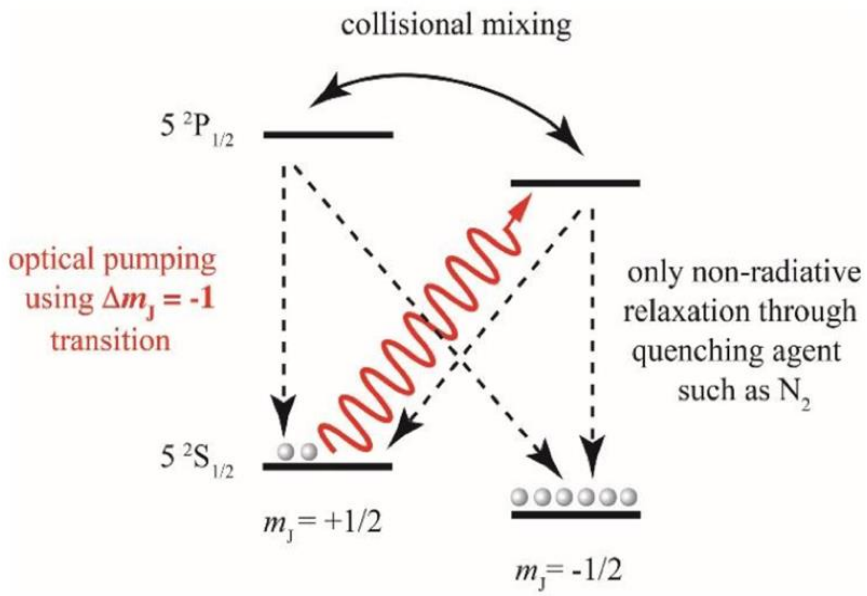

Figure 9: Diagram of Optical Pumping of Rb D1 transition. Eills et al., Chem. Rev. 2023 [15].

In collisions of Rb-Xe atoms, the angular momentum of electron spins of the optically pumped Rb atoms are transferred to nuclear spin of ^{129}Xe atoms through Fermi intervention contact, as shown in Figure 10. Theoretically, three-body collisions are of high-probability spin exchange because the presence of nitrogen atoms in the mixture can lead to the formation of a short-lived van der Waals complex. Yet in our system, we have incorporated a pressure broadening gas, ^{4}He, to broaden the Rb absorption spectrum in order to achieve an improved overlap with the broad spectral emission

profile of the AlGaAs diode lasers. This means that our system enters into a collisional regime where molecules break up very quickly. Consequently, the primary mechanism for spin exchange in our system occurs via two-body collisions between Rb and Xe atoms. Although these collisions lead to a relatively lower alkali spin polarization, the utilization of ^{4}He broadening enables the polarization of a much greater number of Rb atoms, estimated to be 60 times larger than that attainable under low pressure conditions without ^{4}He broadening [12]. This is because if we didn't broaden the Rb absorption line profile, 99% of our laser light would fall outside the Rb resonance and just pass right through. Note that the depolarization of Rb atoms only occurs through collisions with Xe atoms, which is the underlying reason for using a dilute mixture of 1% Xe, 10% N2, and 89% 4He. The N2 and 4He collisions have minimal impacts on Rb spins.

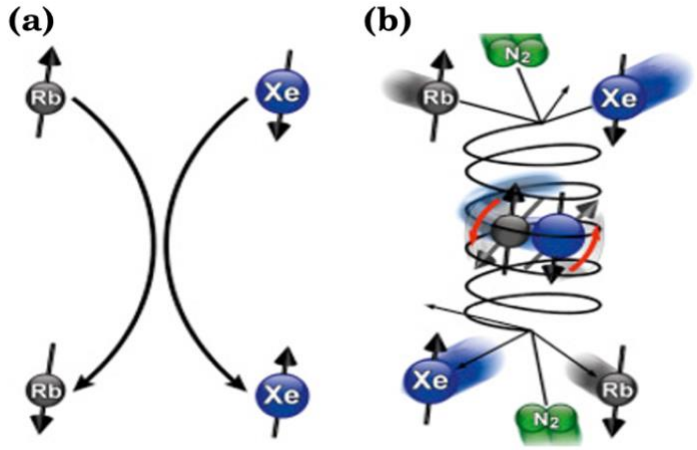

Figure 10: Spin exchange between Rb electron and Xe nuclear spin (a) Binary collisions (b) Three-body collision. Goodson et al., Hyperpolarized and Inert Gas MRI, 2017 [16].

The Xe atoms are then highly polarized. The rubidium vapors condense in the glass tubing as the gas phase mixture leaves the optical pumping chamber. The rate of gas flow is regulated by means of a needle valve to ensure that a ^{129}Xe atom remains in the optical pumping chamber for multiple exchange periods, resulting in its high polarization prior to exiting. Then, the hyperpolarized ^{129}Xe is accumulated in the cold finger with liquid nitrogen (77 K). The polarization of ^{129}Xe remains intact even after freezing. Moreover, the solid ^{129}Xe exhibits a relaxation time that strongly depends on temperature, lasting for about three hours at 77K. The accumulation is limited by the spin lattice relaxation time T1 of the solid phase ^{129}Xe.

Driehuys et al. derived an expression denoting the level of hyperpolarized spin polarization of ^{129}Xe dose is given by P_{Xe}, as presented in equation (2.7).

$$P_{Xe}(t_a) = < P_{Rb} > (\frac{T1}{t_a})(1 - e^{-\frac{t_a}{T1}})(1 - e^{-\frac{[Xe]V_p\gamma_{se}}{F_{Xe}}}), \qquad (2.7)$$

This equation incorporates several factors, including the accumulation time(t_a), average spin polarization of rubidium vapors ($< P_{Rb} >$), xenon flow rate (F_{Xe}), Xe atom density ([Xe]) in the optical pumping chamber, volume of the optical pumping chamber (V_p), and rate of polarization transfer (γ_{se}) to ^{129}Xe via spin exchange collisions with Rb. Altering the accumulation time and gas flow rate as outlined in the equation (2.7) can yield the desired hyperpolarized ^{129}Xe volume and nuclear spin polarization level. The resulting solid-state ^{129}Xe can be thawed to produce a gaseous dose.

Typically, on an older style of polarizer 116, we set the gas flow rate to around 1.5 SLM and the accumulation time to about 30 minutes. These settings typically result in the accumulation of 450 ml volume of xenon, which is then utilized to prepare the desired HP 129Xe dose for MRS scans.

2.3 Dose Equivalent of HP ^{129}Xe

The signal obtained in a ^{129}Xe MRI/MRS experiment depends on not only the level of polarization, but also the amount of xenon, as well as isotopic fraction of NMR-active nucleus ^{129}Xe. This is given by a quantity called dose equivalent (DE):

$$DE = f_{129} \times P_{129} \times V_{Xe}, \quad (2.8)$$

This formula incorporates three key variables: f_{129}, P_{129}, and V_{Xe}. The first variable, f_{129}, represents the isotopic fraction of ^{129}Xe. The second variable, P_{129}, denotes the nuclear spin polarization level of ^{129}Xe. Finally, the third variable, V_{Xe}, corresponds to the volume of xenon in milliliters [17]. Since f_{129} and P_{129} are unitless fractions, the overall unit of DE is milliliters. Thus, DE can be thought of as the equivalent volume of 100% enriched 100% polarized ^{129}Xe.

2.4 Pulmonary Physiology

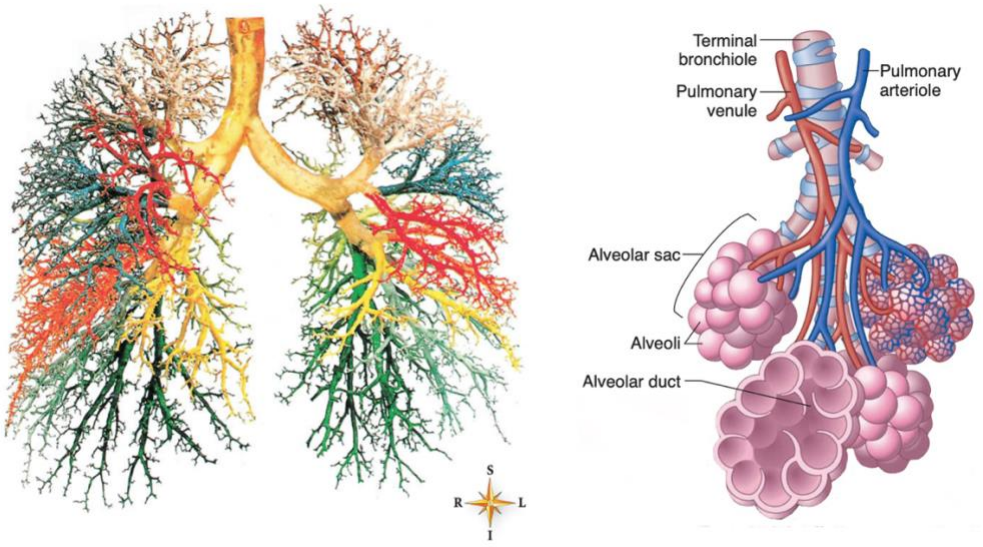

Figure 11: Pulmonary anatomy and physiology. (a) A molded replica of air cavities of the lungs (b) Illustration of alveolar ducts, alveolar sacs. Patton, Thibodeau, Anatomy & Physiology, 2013 [18].

As Xenon atoms penetrate the respiratory system, they traverse a complex network of airways comprising 23 levels of branching within the bronchial tree, ultimately reaching a multitude of minute bronchioles. The Xenon atoms proceed to navigate progressively smaller tubes within these bronchioles, culminating in the microscopic terminal bronchioles, which exclusively facilitate the conduction of air. Subsequently, the xenon atoms continue their journey through the terminal bronchioles and enter the respiratory bronchioles, which are characterized by thin walls that facilitate gas exchange. Finally, the Xe atoms proceed onward into alveolar ducts, which end in one or more alveolar sacs. It is at this point that Xenon atoms dissolve into the lung parenchymal tissue, blood plasma and ultimately into red blood cells in the

pulmonary capillaries around alveolar ducts. An approximation suggests that the total number of alveoli present in human lungs is around 300 million, and it is within these structures that the majority of the dissolved phase signal of HP ^{129}Xe imaging and spectroscopy originates, as shown in Figure 11. Additionally, the gas phase signal is also derived from these alveoli, as well as from 23 branches of airways.

The effects of obstructive and restrictive lung diseases on ^{129}Xe MRS and MRI vary significantly. Chronic obstructive pulmonary disease (COPD) is a widespread pathological condition that is characterized by a gradual decline in airflow and destruction of pulmonary structures, which results in airway gases or particles, primarily present in cigarette smoke, which triggers a chronic inflammatory response and remodeling of the lung architecture [19]. This remodeling process culminates in reduced gas ventilation, leading to low membrane uptake and RBC transfer, ultimately impacting the ventilation and gas exchange functions of the lung. The severity of COPD can vary from being asymptomatic to leading to acute respiratory failure, depending on the extent of damage. In contrast, restrictive lung disease, for example, idiopathic fibrosis (IPF), is characterized by interstitial fibrosis, which results in a gradual loss of pulmonary function and irreversible respiratory failure [20]. Patients with IPF display normal ventilation, but with increased membrane uptake due to interstitial fibrosis, leading to diminished RBC transfer signals, as depicted in Figure 3. Pulmonary arterial hypertension (PAH), a cardiopulmonary disease, often arises from contraction,

remodeling and thrombosis of the small pulmonary arteries and arterioles [21], impacting the RBC concentration in pulmonary capillaries. Patients with PAH display abnormal ^{129}Xe-RBC dissolved phase imaging and ^{129}Xe-RBC spectral signal fluctuations.

2.5 Dose Considerations for HP ^{129}Xe Ventilation Magnetic Resonance Imaging

A past study [17] was conducted in our laboratory to assess the impact of different doses of HP ^{129}Xe on the signal-to-noise ratio (SNR) and conspicuity of ventilation defects in both multi-slice gradient echo (GRE) and isotropic 3D-radially acquired ventilation MRI [14] on a 1.5 T GE Healthcare EXCITE 15 M4 MR scanner. This was achieved by dividing the SNR by the voxel volume, resulting in the normalized SNR_n. It's suggested that SNR_n of ventilation images correlates with dose equivalent. The utilization of a DE value of 71 ml yields an approximate SNR_n of 1.9 ± 0.8 ml^{-2} for a GRE scan with a resolution of for 4x4x12.5 mm. In the contrast, the use of a DE value of 24 ml results in an approximate SNR_n of 0.8 ± 0.2 ml^{-2} for the same GRE scan resolution. A comparison was made between 3D radial images and multi-slice gradient echo (GRE) images, which showed that the SNR achieved by radial imaging was lower than that achieved by conventional GRE.

It's important to take note that the recent FDA approval for ventilation imaging requires a minimum approved DE of 75 ml with a resolution of 4x4x15 mm.

Notably, although the relationship between SNR and DE has been firmly established for imaging of ventilation, the same was not affirmed for gas exchange

spectroscopy, or imaging in general. Furthermore, the study did not address a correlation between dose equivalent and signal quality of HP ^{129}Xe MRS scans.

3. Methods

Prior to this study, there was a notable absence of research that had conducted identical scans at a wide range of doses to establish the relationship between dose equivalent and signal-to-noise ratio (SNR) in hyperpolarized ^{129}Xe magnetic resonance spectroscopy. This study aims to address this gap in knowledge by presenting methods to evaluate the correlation between a broad range of HP ^{129}Xe dose equivalent and the SNR of HP ^{129}Xe MRS scans. Additionally, the aim is to ascertain the necessary dosage of HP ^{129}Xe for spectroscopy scans to meet acceptable standards.

To achieve this objective, HP ^{129}Xe MRS was performed on 85 subjects, including 21 healthy subjects and patients across different age, sex, and disease groups. The patient groups consisted of 33 idiopathic pulmonary fibrosis (IPF) patients and 31 patients with other obstructive and restrictive lung diseases, including long haul COVID, pulmonary hypertension, chronic obstructive pulmonary disease (COPD), chronic hypersensitivity pneumonitis, interstitial lung disease (ILD), Pompe disease, lung transplant, shunt, dyspnea disease, e-cigar, and radiation therapy patients.

3.1 Dose Preparation

In order to conduct clinical studies, isotopically enriched HP ^{129}Xe is obtained using a commercially available polarizer (Model 9810/9820, Polerean, Inc., Durham, NC) by flowing a gas mixture of 1% Xe, 10% N_2, and 89% He through the polarizer. Historically, we have consistently used the isotopic fraction of ^{129}Xe around 86% at the

Xenon MRI Service Center, Duke University. The technique of spin exchange optical pumping, which is expounded upon in section 2.2, is used to highly polarize the isotopically enriched ^{129}Xe. The HP ^{129}Xe is then cryogenically accumulated, thawed, and pumped into a Tedlar bag, as shown in Figure 12. This ^{129}Xe is highly polarized and it constitutes the spectroscopy/imaging component of the administered dose. The remaining portion of the dose encompasses other non-polarized isotopes of xenon and N2, which are incorporated in the dose to balance the volume as needed.

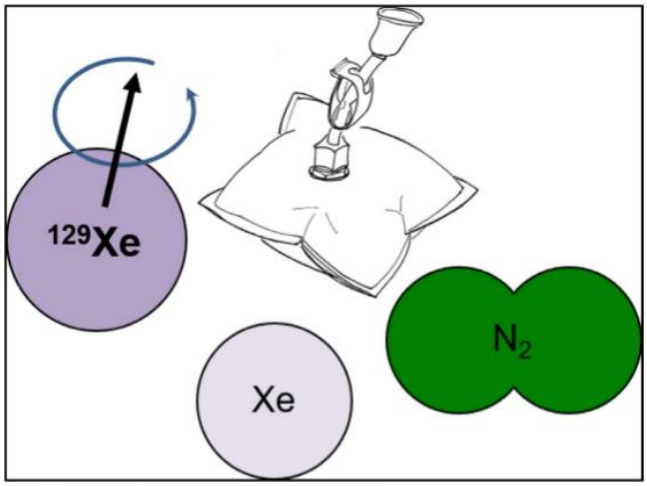

Figure 12: Constituents of a hyperpolarized ^{129}Xe spectroscopy/imaging dose. Nebalski et al., Magnetic Resonance in Medicine, 2021 [21].

We then measure the nuclear spin polarization level of ^{129}Xe using a polarization measurement station (Model 2881, Polarean, Inc., Durham, NC) immediately before administering the dose to the subject.

The computation of the dose equivalent was performed in accordance with the methodology outlined in section 2.3. The dose equivalent volume represents the

equivalent volume of 100% polarized and 100% isotopically enriched ^{129}Xe. In this study, the administered dose equivalents for scans ranged from 50.5 ml to 113.8 ml, with a mean of 82.1±15.1 ml, as illustrated in the Figure 13.

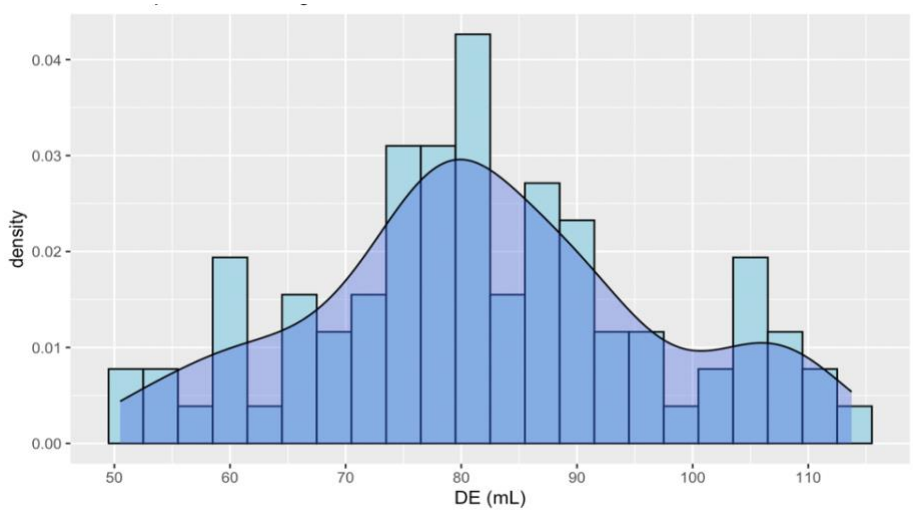

Figure 13: Dose equivalent histogram: Range and Frequency of ^{129}Xe DE used.

3.2 Signal Acquisition and Processing

In this study, patients were instructed to lie on their back and were fitted with a quadrature vest coil. Following initial localizer and proton thoracic cavity scans, ^{129}Xe MRS was performed on patients with a DE range of 50.5 ml to 113.8 ml. During a 7.8 second breathing maneuver, HP ^{129}Xe free induction decay (FID) signals were acquired using a quadrature ^{129}Xe coil, in accordance with the recommendations of the consortium [22], on a 3.0 T Siemens Prisma scanner. The acquisition protocol comprises a 0.69 ms windowed sinc RF pulse, centered on the ^{129}Xe red blood cells (RBCs) resonance, with a 20 degrees flip angle. The repetition time (TR) and echo time (TE) are 15 ms and 450 μs, respectively, while the dwell time is 19.5 μs. The initial frame of the

signal is purely composed of noise, obtained without RF excitation. Subsequently, 500 FIDs are acquired following the excitation of dissolved-phase HP ^{129}Xe in RBCs. The FID signal is captured discretely at 512 time points in each TR. The raw time-domain FID signals obtained from the scanner are saved in a mat file. An illustration of both real and imaginary components of one single FID is shown in Figure 14.

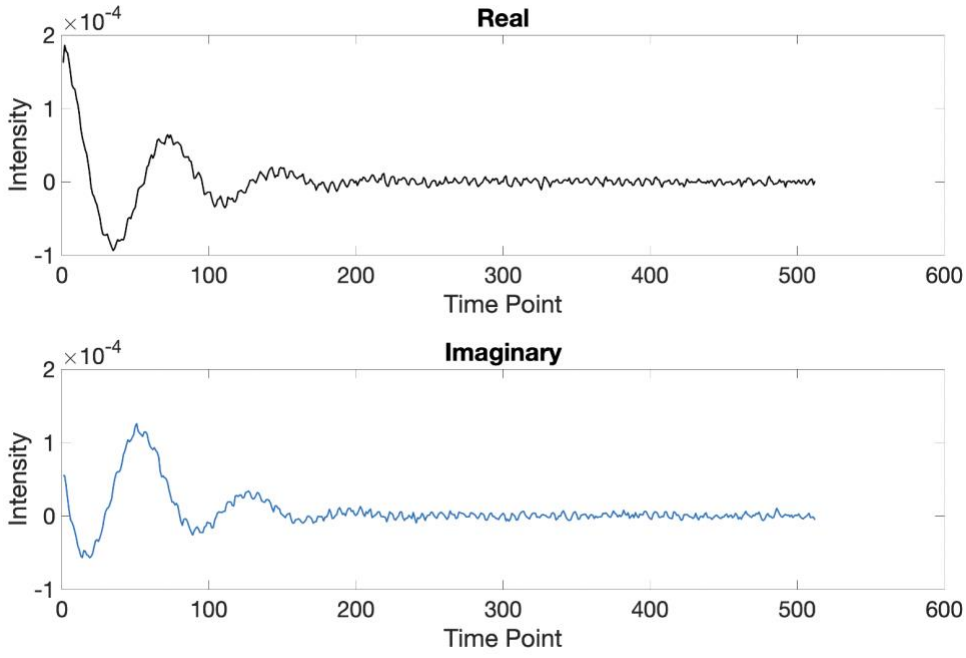

Figure 14: Real and Imaginary components of one single FID.

While the signal is acquired in the time domain, it is common to visualize it in the Fourier domain, to reveal the underlying individual resonances and their shapes, as shown in Figure 15.

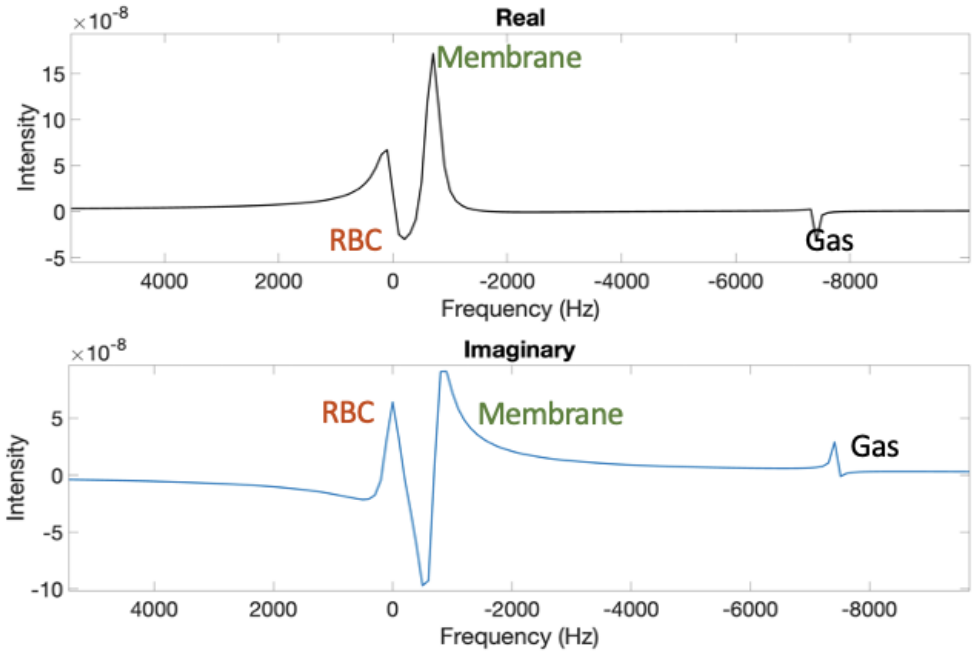

Figure 15: Real and Imaginary Components of ^{129}Xe NMR Spectra: there are RBC, membrane, and gas resonant peaks from high to low frequencies.

In the context of HP ^{129}Xe signal analysis, the FIDs observed over 1 second in the steady state of magnetization undergo a fitting process. This involves performing an accurate fitting procedure in the time domain to extract the individual amplitudes, frequencies, linewidths, and phases [23]. The analysis reveals that the RBC and gas signals can be accurately modeled using a Lorentzian profile, whereas the membrane signal exhibits a more heterogeneous line shape which can be better characterized by a Voigt profile [24]. In this context, the Voigt profile, which is formed by convolving a Gaussian distribution with a frequency Lorentzian curve, is deemed the most appropriate fit for the membrane signal. Notably, the Voigt profile is commonly used in molecular spectroscopy due to its capacity to accurately represent the spectral line

shape. This observation highlights the importance of using an appropriate profile for each component in the analysis to ensure accurate interpretation of the results.

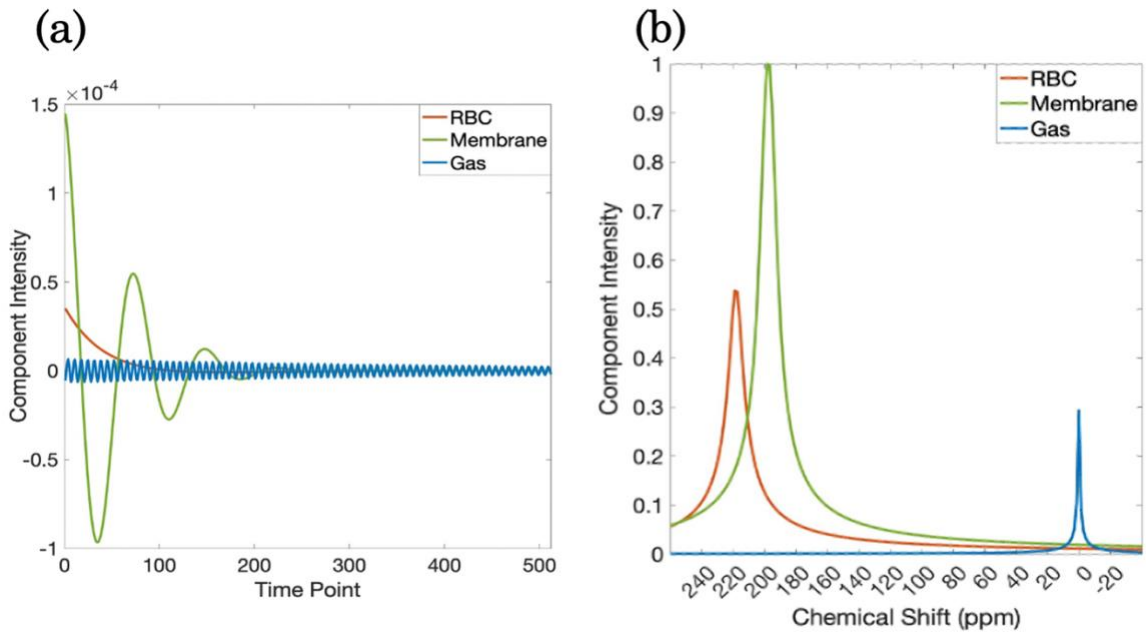

Figure 16: (a) Time domain fitted structure showing red blood cell (RBC), membrane, and gas resonances. (b) Spectral domain.

By utilizing the appropriate profile for each component, the fitting process enables the extraction of the spectral structure of HP ^{129}Xe, which is presented in both time and spectral domains, as shown in the accompanying Figure 16. The spectral domain representation demonstrates the peak positions and widths of various spectral components, while the time domain representation portrays the decay behavior of different components of the signal. The integration of these two representations provides a comprehensive overview of spectral characteristics of HP ^{129}Xe signal. In addition to providing information on the spectral structure, the fitting process further

facilitates the quantification of static spectral biomarkers, such as RBC/Membrane ratio and resonance chemical shifts. The RBC/Membrane ratio is obtained by dividing the signal amplitudes of the RBC and membrane components in the time domain, with the component amplitudes corresponding to the area under component peaks in the frequency spectra.

3.2 Signal-to-Noise Ratio Analysis

The precision and validity of our gathered spectral data hold paramount significance. The presence of noise can considerably affect the accuracy and dependability of the outcomes derived from the data, particularly in HP ^{129}Xe spectra. Two distinct sources contribute to noise in this regard. Firstly, systematic noise originates from the MR scanner and the coil's resistance utilized in the process. Secondly, thermal noise emerges from the human body, which is a common form of noise resulting from thermal fluctuations. Both sources of noise are essentially Johnson noise that arises from the erratic motion of electrons. In conventional MRI/MRS, there are various noise regimes, including coil-noise dominated and body-noise dominated. Typically, proton MRI is wholly dominated by body noise. However, ^{129}Xe MRI/MRS falls in the intermediate category, being neither fully coil-noise nor body-noise dominated.

The objective of signal-to-noise ratio (SNR) analysis was to assess the quality of the data obtained from a 1-second average of 67 FIDs. The data was acquired during a period 2 seconds after the start of the breath-hold to ensure steady-state magnetization.

By subtracting the averaged FID from each individual FID, we obtained a subtraction noise frame for each individual FID. The dedicated noise frame and one example of subtraction noise frame are illustrated in the accompanying Figure 17. The dedicated noise frame was programmed into the sequence to provide a ground truth for system noise. However, we sought to use this information to further develop noise analysis for scans that did not include such a dedicated noise frame by developing the estimated noise frame method [25]. To determine the spectral noise, these two different methods were employed, namely the noise frame signal-to-noise ratio and estimated noise frame signal-to-noise ratio.

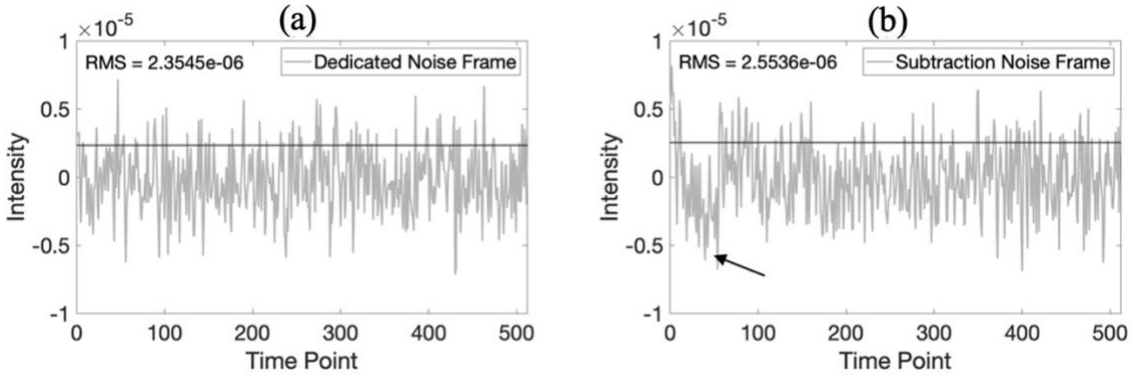

Figure 17: (a) Dedicated noise acquisition frame (b) Noise estimated by subtracting a single FID from average with cardiogenic artifact, as indicated by the arrow.

The estimated noise frame signal-to-noise ratio was determined by calculating the root mean square (RMS) noise of the subtraction noise frame. This value was found to be close to, but slightly higher than, that of the dedicated noise frame due to subtle amplitude differences from the cardiogenic oscillations, as indicated by the arrow. Due to the presence of these subtraction artifacts in the estimated noise frames, only the latter half of the frames was preserved for noise estimation. As a result, only the second half of the subtraction noise frame was utilized for the calculation of the estimated noise frame SNR. These individual estimated noise frames (ENF_i) SNR were then averaged to determine the estimated noise frame SNR.

$$\overline{\mathrm{FID}} = \frac{1}{67}\sum_{i=1}^{67} \mathrm{FID} \qquad (2.1)$$

$$\mathrm{ENF_i} = \overline{\mathrm{FID}} - \mathrm{FID_i} \qquad (2.2)$$

$$\mathrm{SNR_{ENF}} = \frac{1}{\sqrt{67}}\sum_{i=1}^{67} \frac{\text{Amplitude fit } (\overline{\mathrm{FID}})}{std\ dev\ (\mathrm{ENF_i})} \qquad (2.3)$$

The SNR was computed for the membrane and red blood cell (RBC) resonances for a 1-second interval. The correlation between the SNR values obtained from the dedicated and estimated noise-frame approaches was examined, and the results are presented in Figure 18.

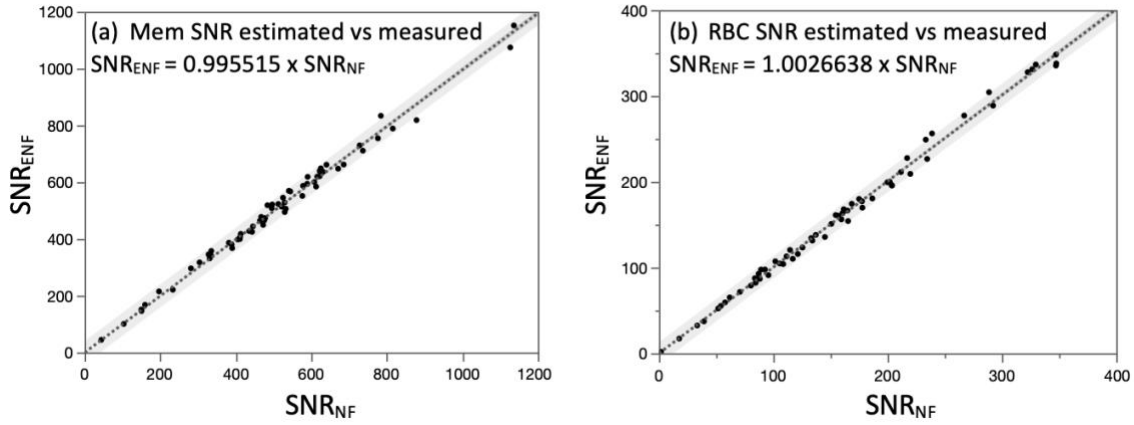

Figure 18: Membrane and RBC measures of SNR are exceptionally well correlated between the estimated- vs dedicated-noise-frame method.

The high correlation coefficient of approximately 1 suggests that there is a strong agreement between the SNR values obtained from both methods. These findings validate the accuracy and dependability of estimated noise frame technique in determining the SNR of the membrane and RBC components.

3.3 Signal-to-Noise versus Dose Equivalent

Finally, the estimated-noise-frame SNR and the administered dose equivalent is correlated against one another for the entire cohort and subgroups of healthy individuals and those with idiopathic pulmonary fibrosis (IPF).

Figure 19 demonstrates the relationship between SNR_{ENF} and DE, for both resonances in the complete cohort and subgroups of healthy individuals as well as those with idiopathic pulmonary fibrosis (IPF). The lighter shade visible on the graph corresponds to the 95% confidence interval pertaining to a specific expected value, while

the darker shade interval indicates the 95% confidence interval associated with the regression line.

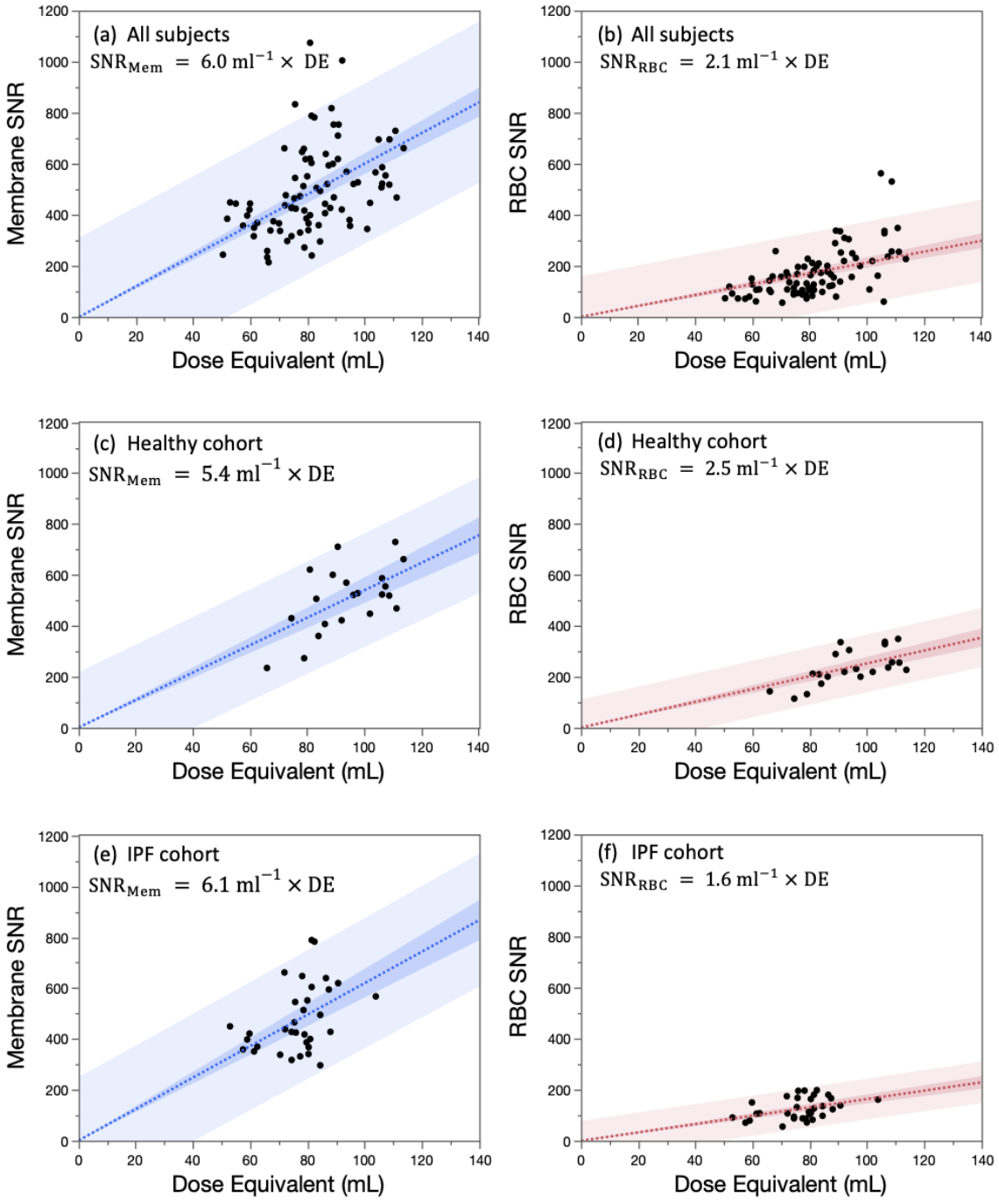

Figure 19: SNR vs dose equivalent for the membrane and RBC components of the ^{129}Xe spectra. (a), (b): SNR scaling across the entire cohort of 88 subjects. (c), (d): SNR scaling for just the cohort of 21 subjects. (e), (f): SNR scaling for a cohort of 33 IPF subjects.

The findings suggest that there is a relationship between SNR_{ENF} and DE for both resonances across the entire cohort. However, the strength of the association differs when examining the healthy and IPF subgroups separately. When evaluating the entire cohort, the correlation between SNR_{ENF} and DE was found to be statistically significant. Moreover, the scatter plot revealed a linear relationship between two variables, as indicated by the darker shade of the plot, which highlights the 95% confidence interval of the regression line. The strength of the association differs when examining the healthy and IPF subgroups separately.

Across the entire cohort, the relationships were:

$$SNR_{Mem} = 6.0\ ml^{-1} \times DE \qquad (3,1)$$

$$SNR_{RBC} = 2.1\ ml^{-1} \times DE \qquad (3,2)$$

These results were similar to what was obtained in the healthy cohort:

$$SNR_{Mem} = 5.4\ ml^{-1} \times DE \qquad (3.3)$$

$$SNR_{RBC} = 2.5\ ml^{-1} \times DE \qquad (3.4)$$

Yet in the IPF cohort, membrane SNR/DE was higher and that of the RBC signal was lower:

$$SNR_{Mem} = 6.1\ ml^{-1} \times DE \qquad (3.5)$$

$$SNR_{RBC} = 1.6\ ml^{-1} \times DE \qquad (3.6)$$

3.4 ^{129}Xe MRS Scan Quality Evaluation

In our laboratory's recent reader study of ^{129}Xe MRS scan quality, we sought to use reader scoring of dynamic and static spectroscopy to better understand the minimum RBC spectral SNR required.

To address this issue, the reader study determined the technique requirements to achieve a reader score of > 3, which was measured using a 5-point Likert scale for both static and dynamic spectroscopy metrics. A cohort of 155 individuals with varied cardiopulmonary disorders underwent a total of 176 ^{129}Xe spectroscopy studies. Each study employed two MRS scans that were conducted using established protocols, as described in section 3.2. Expert readers evaluated each of the 352 scans and provided separated scores for static and dynamic aspects of the study [26]. The static and dynamic MRS was scored using a 1-5 scale (1-unusable, 5-perfect), as illustrated in Figure 20. The readers based their dynamic ratings on a combination of the quality of static spectral fits, dynamic and static SNR, reasonability of the heart rate, and quality of the dynamic oscillations fits.

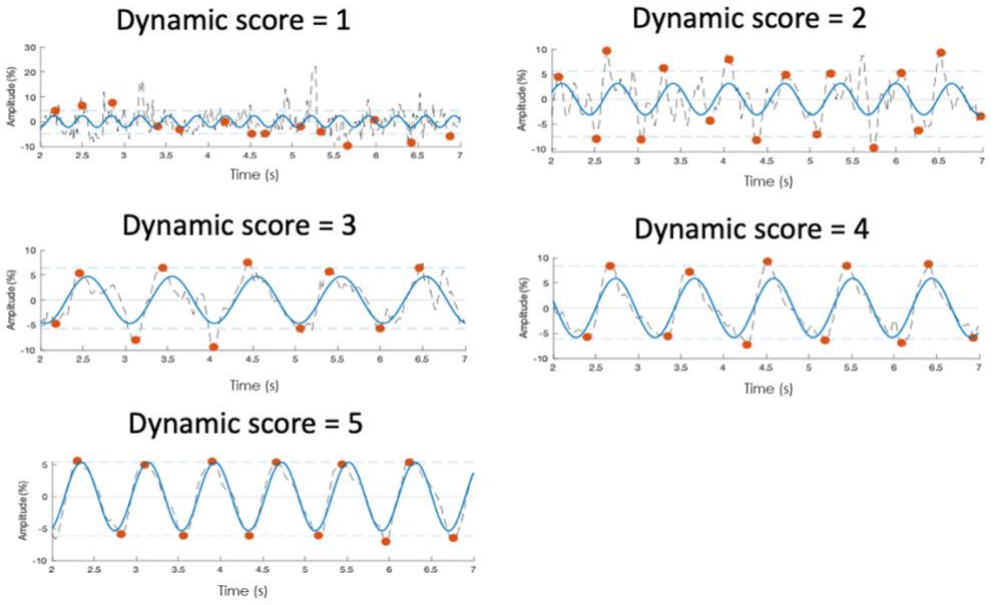

Figure 20: The 5-second temporal pattern of detrended ^{129}Xe-RBC signal amplitude oscillations. Scans are scored by experienced readers on both static and dynamic parameters with 1-5 Likert scale.

Figure 21 displays the box plots of RBC SNR that are grouped by the mean score for static and dynamic components. It is observed that the median RBC SNR for static score of 3 is 26.15, while for dynamic score of 3 is 54.04. With increasing RBC SNR, we observed higher reader scores, for both static and dynamic components. Notably, the RBC SNR requirement for static spectroscopy is lower as compared to its dynamic counterparts, given the same score ranking.

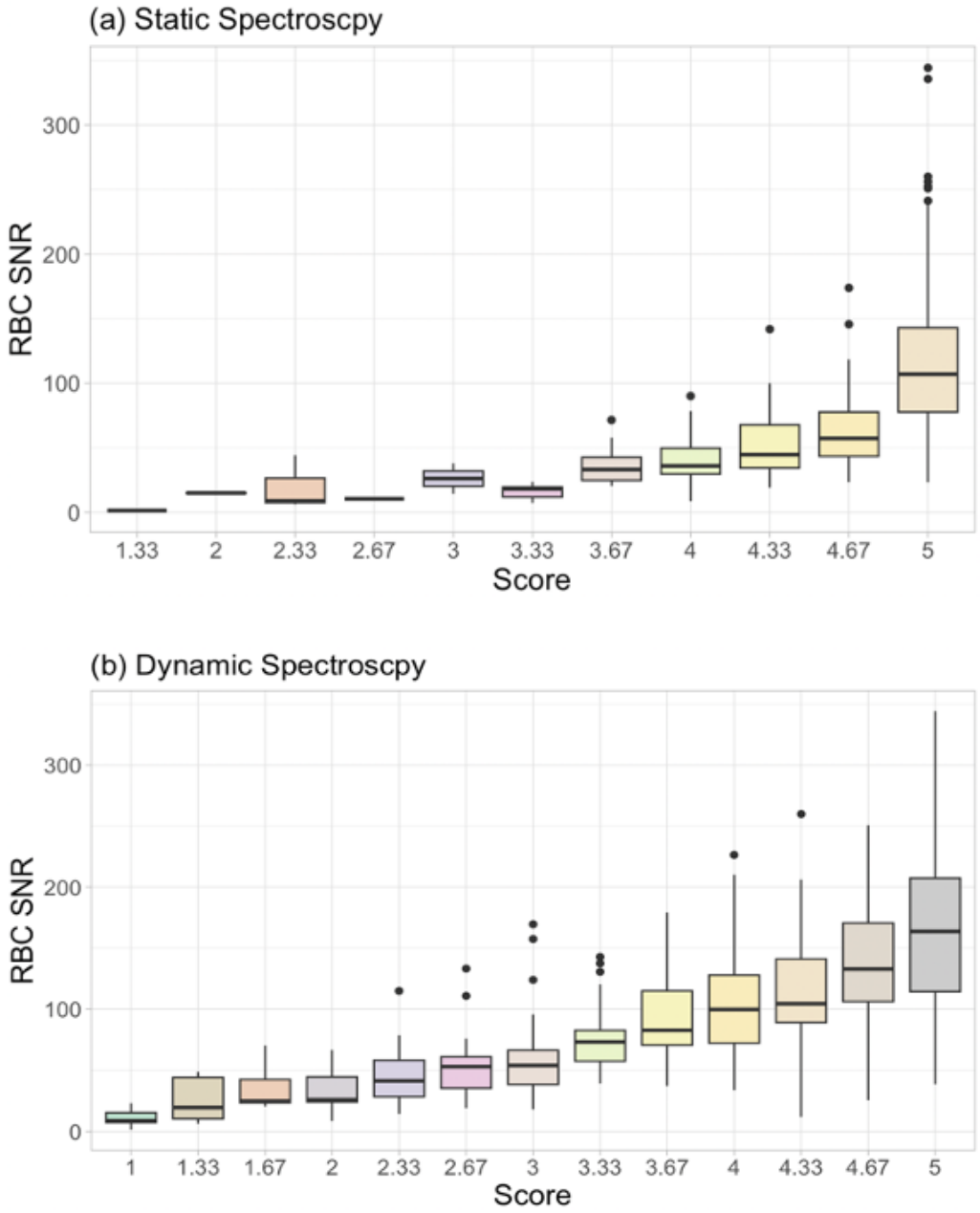

Figure 21: Box plots of RBC SNR grouped by average score for the ^{129}Xe MRS. (a) Static spectroscopy, (b) Dynamic spectroscopy.

4. Results

Our study suggests that the signal-to-noise (SNR) scaling achieved throughout the entire participant cohort is likely adequate for most research purposes. When using a TR of 15 ms and acquiring with a 20-degree flip angle, the SNR of red blood cells (RBCs) is estimated to be approximately 2.1 ml^{-1} DE. We establish a criterion whereby scans with a score of 3 or higher are considered acceptable. Mean RBC SNR values for each score group equal to or above 3 are presented in Figure 22. By averaging the mean RBC SNR values for all score groups with scores equal to or above 3, we determined that an RBC SNR of 50.99 is required for acceptable static spectra, while an RBC SNR of 108.72 is necessary for acceptable dynamic spectra.

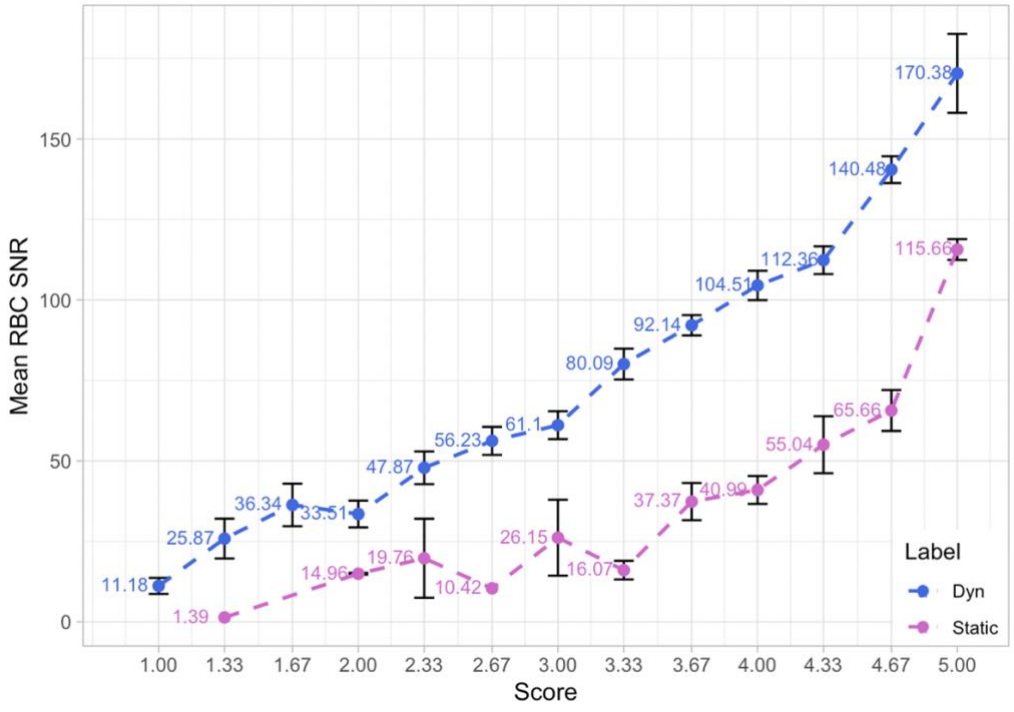

Figure 22: Mean RBC SNR for Each Score Group.

Using the DE scaling here, we suggest DE of 24.3 ± 1.0 ml is required for robust static spectra and 51.7 ± 4.7 ml is required for dynamic spectra.

4. Discussion

This study serves as a valuable contribution to the field of hyperpolarized ^{129}Xe magnetic resonance diagnosis by providing a more comprehensive understanding of the relationship between dose equivalent and SNR in HP ^{129}Xe MRS scans. By including a diverse patient population, this study provides insights into how various patient characteristics may impact this relationship. The findings of this study may have important implications for optimizing the dose of HP ^{129}Xe for MRS scans and ultimately improving the accuracy and diagnoses and treatment planning for pulmonary diseases.

The current study presents a significant contribution towards establishing a standardized approach for the use of hyperpolarized ^{129}Xe magnetic resonance (HP ^{129}Xe MR) spectroscopy in clinical practice. The quantitative measure of signal-to-noise-ratio (SNR) obtained in this study, as well as the establishment of a clear relationship between dose and SNR, can aid in ensuring the consistency and reproducibility of HP ^{129}Xe MR spectra acquisition and analysis across different institutions and studies.

By offering a reliable and quantitative measure of SNR, the approach taken in this study can potentially increase the accuracy and sensitivity of HP ^{129}Xe MR spectroscopy, thereby enhancing its value in clinical practice. Moreover, by establishing a clear relationship between dose and SNR, this study can help optimize the use of HP ^{129}Xe MR spectroscopy in the context of clinical trials and other research studies. Standardizing

the acquisition and analysis of HP ^{129}Xe MR spectra can also facilitate the pooling of data across different studies, thereby enabling larger and more powerful meta-analyses.

This study has important implications for advancing our understanding of pulmonary disease and evaluating the efficacy of new treatments. By providing a more robust method for measuring signal quality, this study can help facilitate future studies aimed at investigating the relationship between HP ^{129}Xe MR spectroscopy and various physiological and pathological processes in the lungs. Moreover, this study can inform efforts to optimize the use of HP ^{129}Xe MR spectroscopy in the context of personalized medicine by identifying optimal dosing strategies for different patient populations, ultimately improving diagnostic accuracy and treatment efficacy.

This study also revealed variation in DE scaling between healthy volunteers and patients with idiopathic pulmonary fibrosis (IPF). Notably, the RBC SNR of the IPF cohort was 1.6 times lower than that of the healthy cohort. This finding is not surprising, given the impaired gas exchange in these patients and the difference in RBC/membrane ratio of approximately 0.46 for the healthy cohort versus ~0.26 in the IPF cohort. This disparity suggests that less ^{129}Xe reaches the RBC compartment of IPF patients for a given DE. On the other hand, IPF patients exhibited higher SNR/DE for the membrane compartment than both the healthy subjects and the entire patient cohort, which is consistent with the known finding that an elevated membrane signal is characteristic of patients with IPF and interstitial pneumonias in general. This is because pulmonary

interstitium is the primary site of pathology in interstitial pneumonia. Previous research has established that the development of interstitial pulmonary fibrosis is caused by excessive deposition of collagen, which restricts the alveoli's capacity to facilitate gas exchange [27]. Thickening of the interstitial membrane, a consequence of interstitial fibrosis, leads to an increased uptake of ^{129}Xe. Furthermore, the thickening of the membrane in affected areas hampers gas diffusion, leading to a decrease in RBC transfer.

We suggest that the SNR scaling achieved across the entire cohort is likely sufficient for most studies. However, it is essential to keep in mind that there are differences in DE scaling between healthy and IPF cohorts. Therefore, researchers should consider these differences when designing and conducting studies of HP ^{129}Xe spectroscopy in patients with IPF. Further research is needed to determine if the observed difference in DE scaling can be used to develop more accurate and reliable biomarkers for IPF diagnosis and monitoring.

5. Conclusions

This study provides a robust means of calculating SNR for ^{129}Xe MRS and establishes its relationship to the administered dose equivalent for the current standard acquisition. We demonstrated that the SNR calculated using estimated noise frame is virtually identical to that obtained with a dedicated noise frame, thus simplifying the acquisition.

The results of the reader study on ^{129}Xe MRS dynamic and static spectroscopy can be practically applied to estimate the required dose equivalent (DE) needed for acceptable quantification of spectroscopic biomarkers. Based on the results, a DE of 25.3 ± 1.0 ml is required for robust static spectra, while 50.2 ± 4.7 ml is required for dynamic spectra, with an SNR of 50.6 and 105.4, respectively. This information may prove useful in future multicenter trials that incorporate ^{129}Xe MRS.

5.1 Limitations

It is important to note that there are limitations to this study. For instance, the cohort size is relatively small, which may limit the generalizability of the findings. Additionally, the study only included individuals with IPF and healthy controls, which may not represent the entire population. Thus, future research should aim to replicate these findings in larger, more diverse populations.

5.2 Future Directions

This section presents a proposal for future research on dose requirements and signal-to-noise-ratio (SNR) of HP ^{129}Xe gas exchange MRI. Additionally, an alternative approach for analyzing HP ^{129}Xe magnetic resonance spectra is suggested. Rather than using the Voigt profile to fit the time domain free induction decay signals, we can correct the phase of the three resonant peaks in the spectra and fitting them with a Lorentzian profile. This method has the potential to offer a comprehensive understanding of the changes in the ^{129}Xe – RBC chemical shifts in response to varying oxygenation levels of pulmonary capillary. It would be valuable if we could relate this pulmonary capillary oxygenation to the true capillary oxygenation of the patient.

References

[1] Wang, Z., Bier, E. A., Swaminathan, A., Parikh, K., Nouls, J., He, M., Mammarappallil, J. G., Luo, S., Driehuys, B., & Rajagopal, S. (2019). Diverse cardiopulmonary diseases are associated with distinct xenon magnetic resonance imaging signatures. European Respiratory Journal, 54(6). https://doi.org/10.1183/13993003.00831-2019

[2] Wang, Z., Rankine, L., Bier, E. A., Mummy, D., Lu, J., Church, A., Tighe, R. M., Swaminathan, A., Huang, Y. C. T., Que, L. G., Mammarappallil, J. G., Rajagopal, S., & Driehuys, B. (2021). Using hyperpolarized 129Xe gas-exchange MRI to model the regional airspace, membrane, and capillary contributions to diffusing capacity. Journal of Applied Physiology, 130(5). https://doi.org/10.1152/japplphysiol.00702.2020

[3] Weatherley, N. D., Stewart, N. J., Chan, H. F., Austin, M., Smith, L. J., Collier, G., Rao, M., Marshall, H., Norquay, G., Renshaw, S. A., Bianchi, S. M., & Wild, J. M. (2019). Hyperpolarised xenon magnetic resonance spectroscopy for the longitudinal assessment of changes in gas diffusion in IPF. Thorax, 74(5). https://doi.org/10.1136/thoraxjnl-2018-211851

[4] Norquay, G., Leung, G., Stewart, N. J., Wolber, J., & Wild, J. M. (2017). 129Xe chemical shift in human blood and pulmonary blood oxygenation measurement in humans using hyperpolarized 129Xe NMR. Magnetic Resonance in Medicine, 77(4). https://doi.org/10.1002/mrm.26225

[5] Hoenderdos, K., & Condliffe, A. (2013). The neutrophil in chronic obstructive pulmonary disease: Too little, too late or too much, too soon? In American Journal of Respiratory Cell and Molecular Biology (Vol. 48, Issue 5). https://doi.org/10.1165/rcmb.2012-0492TR

[6] Bier EA, Alenezi F, Lu J, Wang Z, Mammarappallil JG, O'Sullivan-Murphy B, Erkanli A, Driehuys B, Rajagopal S. Noninvasive diagnosis of pulmonary hypertension with hyperpolarized 129Xe magnetic resonance imaging and spectroscopy. European Respiratory Journal Open Research 2022

[7] Tuder, R. M., Stacher, E., Robinson, J., Kumar, R., & Graham, B. B. (2013). Pathology of pulmonary hypertension. In Clinics in Chest Medicine (Vol. 34, Issue 4). https://doi.org/10.1016/j.ccm.2013.08.009

[8] Galiè, N., Humbert, M., Vachiery, J. L., Gibbs, S., Lang, I., Torbicki, A., Simonneau, G., Peacock, A., Noordegraaf, A. V., Beghetti, M., Ghofrani, A., Sanchez, M. A. G., Hansmann, G., Klepetko, W., Lancellotti, P., Matucci, M., McDonagh, T., Pierard, L. A., Trindade, P. T., … Hoepera, M. (2016). 2015 ESC/ERS guidelines for the diagnosis and treatment of pulmonary hypertension: The joint task force for the diagnosis and treatment of pulmonary hypertension of the european society of cardiology (ESC) and the european respiratory society (ERS): Endorsed by: Association for european paediatric and congenital cardiology (AEPC), international society for heart and lung transplantation (ISHLT). In Russian Journal of Cardiology (Vol. 133, Issue 5). https://doi.org/10.15829/1560-4071-2016-5-5-64

[9] Vachiéry, J. L., & Gaine, S. (2012). Challenges in the diagnosis and treatment of pulmonary arterial hypertension. In European Respiratory Review (Vol. 21, Issue 126). https://doi.org/10.1183/09059180.00005412

[10] Hoeper, M. M., Lee, S. H., Voswinckel, R., Palazzini, M., Jais, X., Marinelli, A., Barst, R. J., Ghofrani, H. A., Jing, Z. C., Opitz, C., Seyfarth, H. J., Halank, M., McLaughlin, V., Oudiz, R. J., Ewert, R., Wilkens, H., Kluge, S., Bremer, H. C., Baroke, E., & Rubin, L. J. (2006). Complications of Right Heart Catheterization Procedures in Patients With Pulmonary Hypertension in Experienced Centers. Journal of the American College of Cardiology, 48(12). https://doi.org/10.1016/j.jacc.2006.07.061

[11] Messiah, A. M. L., & Greenberg, O. W. (1964). Symmetrization Postulate and Its Experimental Foundation-sar Yn-ette (Seine et Oise) France. Physical Review, 136(1B).

[12] Driehuys, B., Cates, G. D., Miron, E., Sauer, K., Walter, D. K., & Happer, W. (1996). High-volume production of laser-polarized 129Xe. Applied Physics Letters, 69(12). https://doi.org/10.1063/1.117022

[13] Kadlecek, S., Magnetic Resonance Imaging with Polarized Gases: Although conventional MRI cannot track inhaled or dissolved gases in the body, physicians may soon be able to do so using specially prepared atoms. American scientist, 2002. 90(6): p. 540-549.

[14] Loudon, R. (1984). Progress in Optics, Vol. XX. Optica Acta: International Journal of Optics, 31(10). https://doi.org/10.1080/713821416

[15] Eills, J.; Budker, D.; Cavagnero, S.; Chekmenev, E.Y.; Elliott, S.J.; Jannin, S.; Lesage, A.; Matysik, J.; Meersmann, T.; Prisner, T.; et al. Spin Hyperpolarization in Modern Magnetic Resonance. Chem. Rev. 2023.

[16] B.M. Goodson, K. Ranta, J.G. Skinner, A.M. Coffey, P. Nikolaou, M. Gemeinhardt, D. Anthony, S. Stephenson, S. Hardy, J. Owers-Bradley, M.J. Barlow, E.Y. Chekmenev, The Physics of Hyperpolarized Gas MRI A2 - Albert, Mitchell S, in: F.T. Hane (Ed.), Hyperpolarized and Inert Gas MRI, Academic Press, Boston, 2017, pp. 23–46, Chapter 2.

[17] He, M., Robertson, S. H., Kaushik, S. S., Freeman, M. S., Virgincar, R. S., Davies, J., Stiles, J., Foster, W. M., McAdams, H. P., & Driehuys, B. (2015). Dose and pulse sequence considerations for hyperpolarized 129Xe ventilation MRI. Magnetic Resonance Imaging, 33(7). https://doi.org/10.1016/j.mri.2015.04.005

[18] Patton, Thibodeau, Anatomy & Physiology, 2013

[19] Singh, D., Agusti, A., Anzueto, A., Barnes, P. J., Bourbeau, J., Celli, B. R., Criner, G. J., Frith, P., Halpin, D. M. G., Han, M., Varela López, M. V., Martinez, F., de Oca, M. M., Papi, A., Pavord, I. D., Roche, N., Sin, D. D., Stockley, R., Vestbo, J., … Vogelmeier, C. (2019). Global strategy for the diagnosis, management, and prevention of chronic obstructive lung disease: The GOLD science committee report 2019. In European Respiratory Journal (Vol. 53, Issue 5). https://doi.org/10.1183/13993003.00164-2019

[20] Barratt, S. L., Creamer, A., Hayton, C., & Chaudhuri, N. (2018). Idiopathic pulmonary fibrosis (IPF): An overview. In Journal of Clinical Medicine (Vol. 7, Issue 8). https://doi.org/10.3390/jcm7080201

[21] Tuder, R. M., Stacher, E., Robinson, J., Kumar, R., & Graham, B. B. (2013). Pathology of pulmonary hypertension. In Clinics in Chest Medicine (Vol. 34, Issue 4). https://doi.org/10.1016/j.ccm.2013.08.009

[22] Niedbalski, P. J., Hall, C. S., Castro, M., Eddy, R. L., Rayment, J. H., Svenningsen, S., Parraga, G., Zanette, B., Santyr, G. E., Thomen, R. P., Stewart, N. J., Collier, G. J., Chan, H. F., Wild, J. M., Fain, S. B., Miller, G. W., Mata, J. F., Mugler, J. P., Driehuys, B., … Woods, J. C. (2021). Protocols for multi-site trials using hyperpolarized 129Xe MRI for imaging of ventilation, alveolar-airspace size, and gas exchange: A position paper from the 129Xe MRI clinical trials consortium. Magnetic Resonance in Medicine, 86(6). https://doi.org/10.1002/mrm.28985

[23] Robertson, S. H., Virgincar, R. S., Bier, E. A., He, M., Schrank, G. M., Smigla, R. M., Rackley, C., McAdams, H. P., & Driehuys, B. (2017). Uncovering a third dissolved-phase 129Xe resonance in the human lung: Quantifying spectroscopic features in healthy

subjects and patients with idiopathic pulmonary fibrosis. Magnetic Resonance in Medicine, 78(4). https://doi.org/10.1002/mrm.26533

[24] Bier, E. A., Robertson, S. H., Schrank, G. M., Rackley, C., Mammarappallil, J. G., Rajagopal, S., McAdams, H. P., & Driehuys, B. (2019). A protocol for quantifying cardiogenic oscillations in dynamic 129 Xe gas exchange spectroscopy: The effects of idiopathic pulmonary fibrosis. NMR in Biomedicine, 32(1). https://doi.org/10.1002/nbm.4029

[25] Nalcioglu, O., & Cho, Z. H. (1984). Limits to signal-to-noise improvement by FID averaging in NMR imaging. Physics in Medicine and Biology, 29(8). https://doi.org/10.1088/0031-9155/29/8/005

[26] Bechtel, A., Costelle, A., Bier, E., Lu, J., Mammarappallil, J., Kabir, S., Mummy, D., Driehuys, B. (2023). Repeatability of pulmonary 129Xe static spectroscopy and dynamic spectroscopy fit methods: a reader study, ISMRM Abstract

[27] Wang, J. M., Robertson, S. H., Wang, Z., He, M., Virgincar, R. S., Schrank, G. M., Smigla, R. M., O'Riordan, T. G., Sundy, J., Ebner, L., Rackley, C. R., McAdams, P., & Driehuys, B. (2018). Using hyperpolarized 129Xe MRI to quantify regional gas transfer in idiopathic pulmonary fibrosis. Thorax, 73(1). https://doi.org/10.1136/thoraxjnl-2017-210070